

Enhanced One-Photon and Two-Photon Amplified Spontaneous Emissions of CsPbBr₃ Thin Films by Insulating Polymer Coating

Jianshu Liang, Yang Li and Zhouyi Guo*

SATCM Third Grade Laboratory of Chinese Medicine and Photonics
Technology & Guangdong Provincial Key Laboratory of Laser Life Science
College of Biophotonics
South China Normal University Guangzhou
Guangdong 510631, P. R. China
*ann@scnu.edu.cn

Received 21 February 2021

Accepted 17 July 2021

Published 27 August 2021

Lead halide perovskite is an attractive candidate for fabricating low-cost one-photon and two-photon-pumped lasers. However, the presence of vast trap sites and the leakage of electric fields limit the efficient amplified spontaneous emission (ASE) performances. Herein, we show that incorporating an insulating polymethylmethacrylate layer with a proper thickness onto perovskite films can play an important role in not only reducing both one-photon and two-photon ASE thresholds but also improving the light exposure stability remarkably. By means of spectroscopic investigation and optical simulation, the enhancement was ascribed to the trap passivation and electric field restraint and improved light outcoupling due to the dielectric confinement by the formation of symmetric waveguides structure. This work indicates the possibility of simple and effective approaches to realize efficient ASE and lasing.

Keywords: Perovskites; PMMA; amplified spontaneous emission; threshold.

1. Introduction

Lead halide perovskites have aroused great attention in recent years due to their excellent optoelectronic properties, such as the high-charge diffusion length,^{1,2} tunable bandgap¹ and feasibly high photoluminescence quantum yield (PLQY).^{4,5} They have been extensively studied for developing high-efficiency electric-light conversion devices, such as perovskites solar cells⁶ and light-emitting diodes (LEDs).⁷ It was also found that perovskites can

display amplified spontaneous emission (ASE)⁸ behavior when excited at pulsed wave or even continuous wave lasers in various perovskite nanostructures, such as nanocrystals (NCs),⁹ nanoribbons,¹⁰ nanowires,^{11,12} nanoplates,¹³ quantum dots¹⁴ and quasi-two-dimensional.¹⁵ Their potential advantages like wavelength tunability, low-lasing threshold and high optical gain make the perovskites a promising candidate for next-generation semiconductor lasing devices. Because of the absence of organic and inorganic interfaces and

*Corresponding author.

interactions, all-inorganic lead halide perovskites (APbX_3 , A = metal ions, X = Cl, Br and I) might have better phase stability, and thus potentially longer operational lifetimes than organic–inorganic hybrid perovskites.

To get high-performance perovskite-based devices, trap engineering is a general and vital issue. For electric-to-light conversion devices, regardless of spontaneous emission, ASE and lasing devices, trap passivation is similarly important. This is due to the imperfect structures of perovskites as fabricated. The pristine CsPbX_3 thin films also suffer from rapid degradation, which results from the effect of heat,¹⁶ water¹⁷ and oxygen.¹⁸ Poor stability is one of the most critical obstacles to commercialize perovskite-based devices. It is another general issue for all perovskite-based devices, like solar cells, LEDs and lasers. One of the widely used strategies is introducing insulators with perovskites to get better device efficiencies as well as improved stability. Wang *et al.* reported that a thin layer of polymethylmethacrylate (PMMA) was inserted between $\text{CH}_3\text{NH}_3\text{PbI}_3$ and Spiro-OmeTAD, and they obtained solar cells with a PCE of 18.1% and less than 5% degradation after 20 days.¹⁹ Bi *et al.* demonstrated a high-quality perovskite film with a PCE greater than 21% by employing PMMA as an antisolvent during the spin coating process, inducing nucleation and growth of perovskite crystals.²⁰ Yang *et al.* reported ethyl cellulose could be introduced into the perovskite layer in solar cells and obtain an improvement of efficiency, hysteresis and stability.²¹ He group reported that the core-shell supra-structures from *in-situ* growth of CsPbBr_3 perovskite NCs by using amphiphilic copolymer had a PLQY that surpasses 60%.²² Efforts also had been made for improving the stability of perovskite active layer,²³ and thus reducing the ASE threshold.^{24–27} Li *et al.* reported CsPbBr_3 :ZnO films have a more compact and smoother surface and reduced ASE threshold significantly.²⁸ Riedl and co-authors recently reported efficient light emission from CsPbX_3 perovskites with a high PLQY of 68% and low-threshold ASE at room temperature by means of thermal imprint. Moreover, they demonstrated distributed feedback and vertical-cavity surface-emitting lasers with ultralow thresholds at room temperature that are not based on nanoscale perovskite crystals.²⁹ In contrast to solar cells and LEDs that are generally operated at relatively low excitation intensities,

ASE and lasing devices worked at very high pump energy densities. The high density of excitons and/or free charge carriers can lead to concentration-induced quenching, which is a phenomenon broadly observed in both organic and inorganic-based materials and devices. Thus, the energy loss pathways and materials stability at a high excitation concentration should be different as the cases at a low-intensity excitation. The requirement for suppressing the trap formation and stability under strong excitation is thus much more severe for ASE devices. Two-photon lasing from colloidal CsPbX_3 NCs was demonstrated previously.^{30,31} In contrast to one-photon scenario, two-photon excitation can be pumped at longer wavelength at red and infrared regions, which can increase pump/imaging depth, thus avoiding the surface defect-related influence of materials. Two-photon gain medium can be easily pumped by economical, commercial diode sources.

Here, by simply depositing a polymer layer (PMMA) on the solution-processed CsPbBr_3 thin film, we have achieved notably enhanced ASE properties under one-photon and two-photon pumpings. It is disclosed that the thickness of the PMMA layer can have significant effects on the resulting performances. Spectroscopic characterizations, like steady-state and transient Photoluminescence (PL) and absorption techniques, were performed to probe the underlying mechanisms. The reduced threshold and enhanced intensity of one-photon/two-photon ASE can be attributed to the trap passivation and optical confinement by PMMA coating. Meanwhile, the photostability of CsPbBr_3 thin film coated with a proper thickness of PMMA was improved under long-time laser irradiation at ambient environment.

2. Experimental Section

2.1. Materials

Cesium bromide (CsBr, 99.9%) and lead bromide (PbBr_2 , 99.9%) were purchased from Sigma-Aldrich (Shanghai, China). The solvent dimethyl sulfoxide (DMSO) and chlorobenzene with an analytical purity were supplied from Diamond (Sangon Biotech, Shanghai, China) and Guangzhou Chemical Reagent Factory (Guangzhou, Guangdong, China), respectively. PMMA (Mw = 550 000) was bought from Alfa Aesar. All solvents and chemicals were used as received without any further purification.

2.2. Synthesis of CsPbBr_3 thin films

The quartz glasses were ultrasonically cleaned using deionized water, ethanol and isopropanol separately two times. 0.3 M CsPbBr_3 precursor solution was prepared by adding CsBr and PbBr_2 with a molar ratio of 1:1 into the 2-mL DMSO solvent. The resulting precursor solution was stirred at 70°C for 1 hour and then remained being stirred overnight at room temperature. CsPbBr_3 thin film was prepared via one-step method, as shown in Fig. 1(a). 65 μL CsPbBr_3 precursor was deposited on the glass by spin-coating subsequently at 1200 rpm for 10 s and 2500 rpm for 120 s. Then, the sample was heated at 70°C for 30 min to form the CsPbBr_3 film with a thickness of about 80 nm. The PMMA layer with a different thickness was, respectively, deposited atop by spin-coating its chlorobenzene solution (5, 10, 15, 20, 25 and 30 mg/mL) at 2000 rpm for 30 s. The thickness of PMMA was measured to be about 20, 50, 70, 110, 160 and 215 nm, respectively, by using a profile meter (Dektak XT; Bruker). The crystallinity was characterized by X-ray diffraction (XRD; X'Pert PRO MPD). The microstructures of perovskite films were investigated by using a scanning electron microscope (SEM; Merlin).

2.3. Spectroscopy characterization

Ultraviolet-visible (UV-vis) absorption spectra were measured by a spectrophotometer (UH5300;

HITACHI). Photoluminescence emission spectra were measured by a CCD spectrometer (IsoPlane; Princeton Instruments). Fluorescence lifetime measurement was taken by using a supercontinuum source laser (SC-PRO; YSL Photonics) with a pulse duration of 100 ps and a repetition rate of 5 MHz as an excitation light source. The fluorescence was focused on the monochromator and then analyzed by a photomultiplier tube detector combined with a Time-Correlated Single Photon Counting system (HydraHarp 400; PicoQuant). ASE measurements were performed by utilizing a femtosecond laser with 120 fs and a repetition rate of 1 kHz (400 nm for one-photon and 800 nm for two-photon ASE measurements).

2.4. Transient absorption measurement

Time-resolved transient absorption was conducted by using a femtosecond laser with a pulse width of 120 fs and a repetition rate of 1 kHz (Spectra-Physics Spitfire). The fundamental frequency light with a wavelength of 800 nm passes through the $\beta\text{-BaB}_2\text{O}_4$ crystal and becomes 400 nm by a second-harmonic generation effect. The 800 nm and 400 nm beams were used as the pump source for the two-photon and one-photon experiments, respectively. A small portion of the 800 nm beam was focused onto a 10-mm sapphire plate to generate a white light continuum which acts as the probe beam.

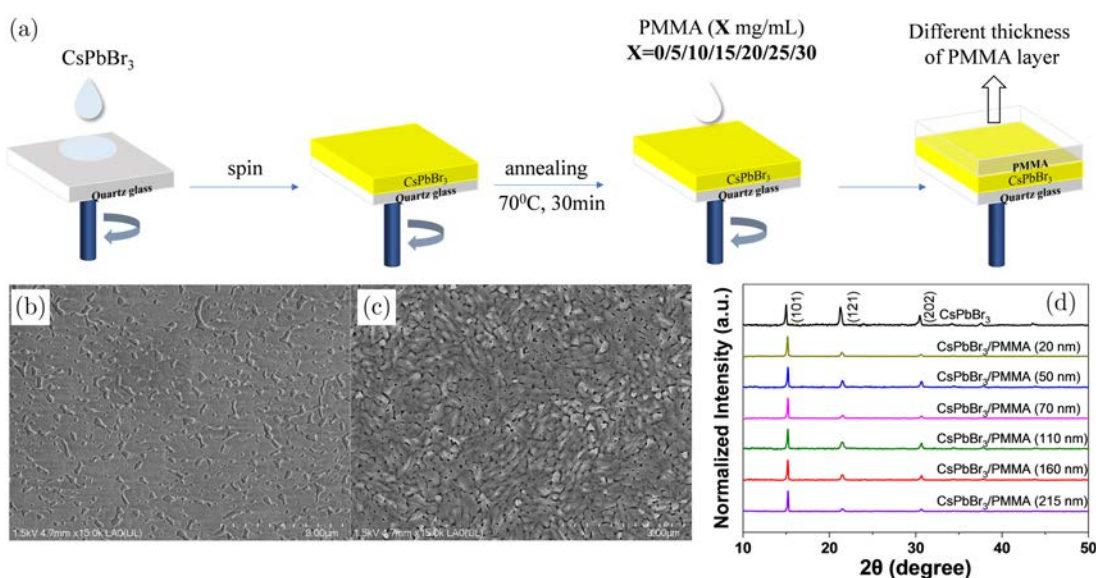


Fig. 1. (a) Schematic diagram of the preparation of the CsPbBr_3 film with PMMA, (b, c) SEM images, and (d) XRD patterns of $\text{CsPbBr}_3/\text{PMMA}$ (x nm) films.

The pump beam ($\sim 400 \mu\text{m}$) was focused onto the film and overlaps with the smaller-diameter probe beam ($\sim 250 \mu\text{m}$). The delay time between the pump beam and the probe beam was controlled by a motion controller (ESP301; Newport). The pump beam was modulated by using an optical chopper (MC2000B; Thorlabs) at a frequency of 500 Hz. The transmittance is acquired as a function of delay time between pump beam and probe beam by using a monochromator (Acton SP2150i; Princeton Instruments) with a CCD (S15351; Hamamatsu). An optical shutter (SC10; Thorlabs) is also used to help measuring the background light and fluorescence, which act as reference signals. Beam power was measured by an optical power meter (918D; Newport). All the experiments were performed at room temperature.

3. Results and Discussion

To systematically study the influence of PMMA coating, we have prepared CsPbBr_3 (80 nm)/PMMA (x nm) bilayer films with six different thicknesses ($x = 0, 20, 50, 70, 110, 160$ and 215). These CsPbBr_3 thin films were prepared via a one-step process, as shown in Fig. 1(a). Details are elaborated in the Synthesis of CsPbBr_3 Thin Films in Experimental Section. As displayed in Fig. 1(b), the CsPbBr_3 film exhibits a rough surface with significant crystal boundaries. These boundaries can be filled by the PMMA coating [Fig. 1(c)]. The XRD patterns of all samples prove the identical locations of diffraction peaks in Fig. 1(d), indicating the coating of the PMMA layer does not change the crystal structure of perovskites. These feature diffraction peaks match well with the orthorhombic symmetry crystal structure of CsPbBr_3 as previously reported.³² The dominant diffraction peaks located at 15.19° , 21.50° and 30.67° are corresponding to (101), (121) and (202) crystal planes, respectively. It is obvious that the relative diffraction peak intensities between (101) and (121) facets are different for samples with and without PMMA. The peak intensity at 21.50° is significantly stronger than the samples with PMMA. This suggests that the incorporation of PMMA changes the periodic alignment of (121) CsPbBr_3 crystal facets significantly.

The absorption spectra of CsPbBr_3 /PMMA films are shown in Fig. S1. An obvious absorption peak at 516 nm can be seen for all samples, indicating that the excitonic transition occurs in similar frequencies.

However, different absorption tails along the red-shift direction of the peak at 516 nm can be observed (noting that a constant background might be contained, which will not affect the following analysis). With the thickness of PMMA increasing from 20 to 70 nm, the absorption tail gradually decreases and nearly disappears for the sample with 70-nm thick PMMA. For the thickness of PMMA from 110 to 215 nm, an additional absorption band appears again. For the sample with 215 nm, an additional, broad absorption peak at around 600 nm can be identified. Since PMMA is totally transparent in this wavelength range, this tail is not from PMMA absorption. The absorption of these samples may be affected by the scattering effect. As previously shown by the SEM measurement, incorporation of PMMA layer significantly changes the surface morphology of the perovskite/PMMA layer. This leads to different scattering effects for the samples with various thicknesses of PMMA. The combined effects from scattering and absorption give different shapes of the absorption tails.

One-photon PL (1PPL) and two-photon PL (2PPL) spectra are shown in Fig. 2. The narrow emission band peaking at around 522 nm with a full width at half maximum (FWHM) of about 18 nm was observed for all samples under both 1PPL and 2PPL excitations, indicating that the de-excitation routines are the same for these two scenarios. The transitions peaking at 525 nm are corresponding to the excitonic absorption peak at 516 nm. There are no emission bands that are responsible for the band-tail absorption. The PL intensity changes notably for the samples with and without PMMA in both 1PPL and 2PPL. The intensities of the emission peaks are extracted to give the PL enhancement factors in the function of the PMMA thickness (Fig. 2(c)). A hump shape can be seen, suggesting that the thickness of PMMA at the range around 70–110 nm is an optimized condition. This indicates that PMMA has been introduced to reduce defect state density and suppress trap-assisted charge recombination.^{21,33} One of the samples with a PMMA layer was tested under two-photon excitation condition in the function of different pump powers. The PL intensity in CsPbBr_3 /PMMA (160 nm) shows a quadratic power dependence (Fig. S2), confirming that the primary excitation pathway for 2PPL experiments is two-photon absorption.

The transient PL decay characteristics probed at the peak wavelength of 522 nm are shown in

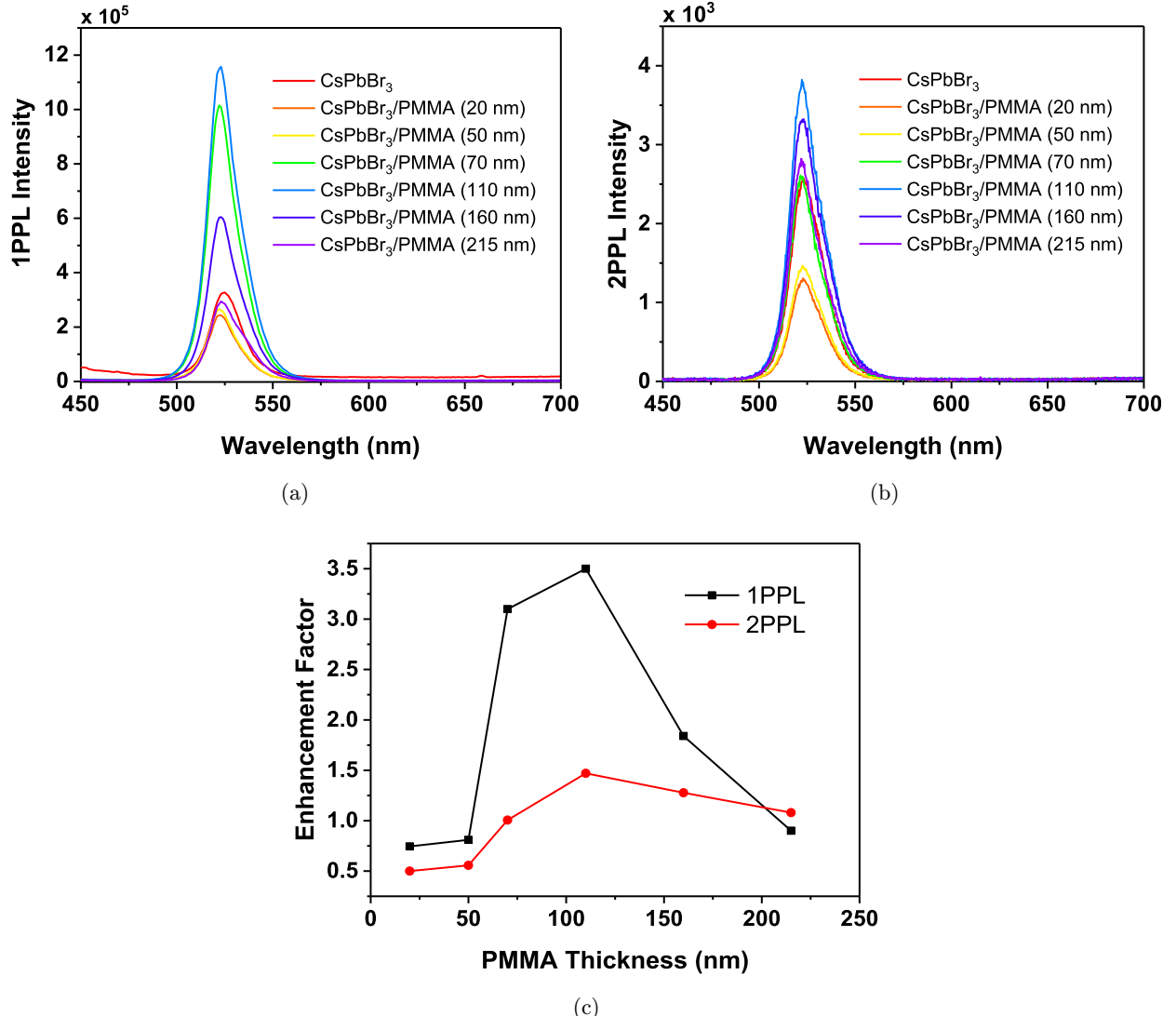


Fig. 2. (a) 1PPL emission, (b) 2PPL emission of the $\text{CsPbBr}_3/\text{PMMA}$ samples, and (c) emission intensity enhancement factors of the samples with a PMMA layer in contrast to the control sample CsPbBr_3 versus the PMMA thickness.

Fig. 3(a). A biexponential decay fitting is conducted to model the lifetime of each film. The fitting results are summarized in Table S1. The average lifetimes (τ_{avg}) of each sample versus the thickness of the PMMA layer are shown in Fig. 3(b). A similar trend like a hump of τ_{avg} can be observed as the changing trend of PL enhancement factors [Fig. 2(c)]. This indicates that the effectiveness of a PMMA coating should be thickness-dependent. The obvious extension of lifetime with a proper PMMA layer indicates that the PMMA coating contributes to passivating the defects that lead to a shorter lifetime of excited states.

Compared with spontaneous emission normally working at a low concentration of excited states, the

ASE needs a rather highly excited fluence. In order to explore the concentration-dependent dynamics of the energy loss in femtosecond timescale, we conducted the femtosecond Transient absorption (TA) measurement of CsPbBr_3 and $\text{CsPbBr}_3/\text{PMMA}$ (160 nm) samples pumped with 400 nm laser with low fluence and high fluence of 25.5 and 122.3 $\mu\text{J}/\text{cm}^2$, respectively. As we will show later, the ASE threshold is between these fluences. The contour plots of the femtosecond TA results are shown in Fig. 4. The spectral evolution characteristics are extracted and shown in Fig. S3. Three negative absorption bands appear which are peaking at around 515, 526 and 547 nm, respectively. The emission bands at around 515 and 547 nm are

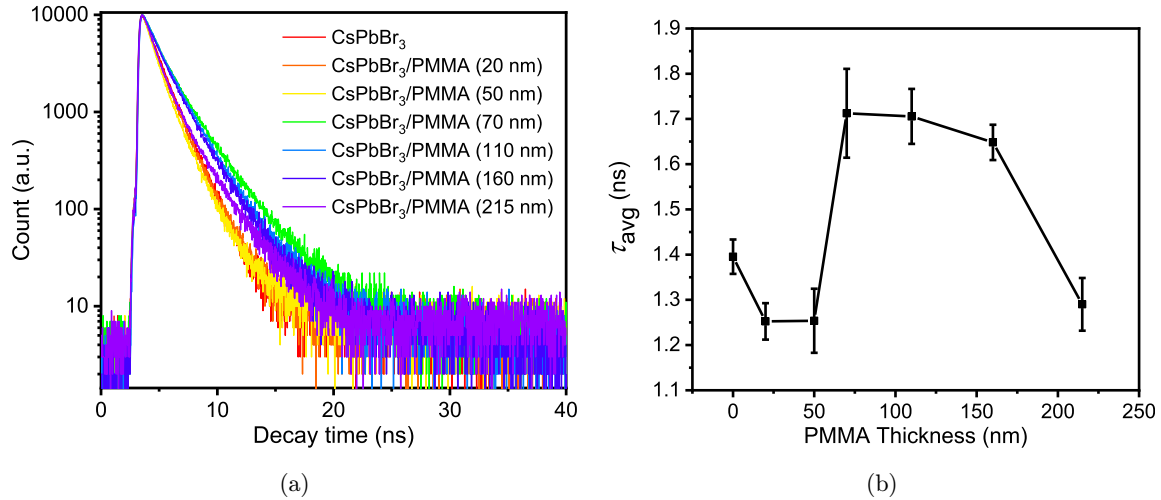


Fig. 3. (a) PL decay characteristics probed at 522 nm and (b) the average lifetime (τ_{avg}) of different films in the function of the PMMA thickness.

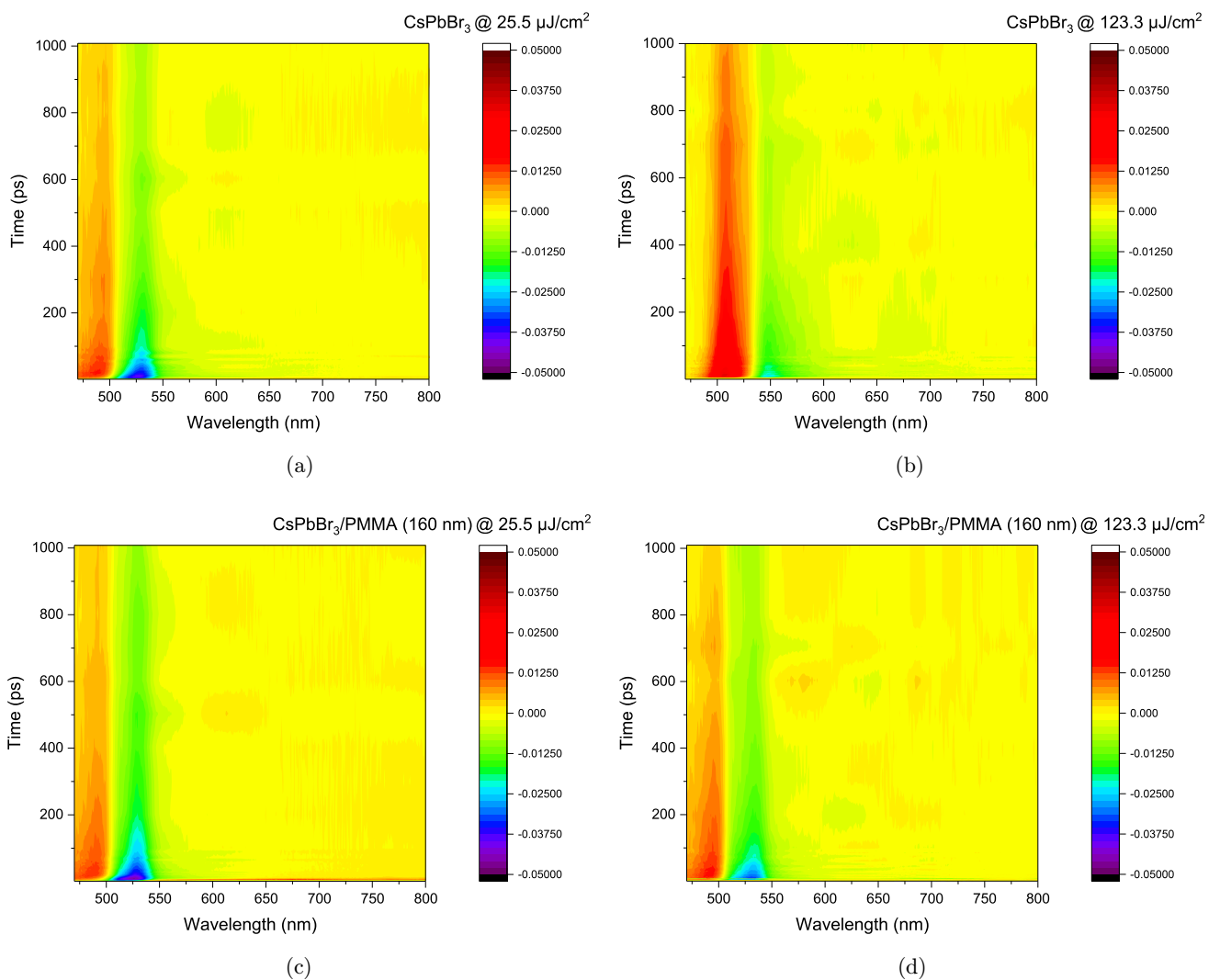


Fig. 4. Contour plots of femtosecond transient absorption of CsPbBr₃ pumped under a fluence of (a) 25.5 $\mu\text{J}/\text{cm}^2$ and (b) 123.3 $\mu\text{J}/\text{cm}^2$, and CsPbBr₃/PMMA (160 nm) pumped under a fluence of (c) 25.5 $\mu\text{J}/\text{cm}^2$ and (d) 123.3 $\mu\text{J}/\text{cm}^2$, respectively.

ascribed with ground-state bleaching (GSB), and the band at around 526 nm arises from stimulated emission and is overlapped with the GSB signal. The CsPbBr_3 sample exhibits different TA behaviors under low-pump and high-pump fluences. At high fluence, the negative bands at 515 and 526 nm disappear. Instead, a red-shifted and broaden photoinduced absorption was present. This indicates that the CsPbBr_3 crystal structures are strongly destroyed and photoinduced species are generated. It is interesting that GSB signal at around 547 nm still exists and a clear negative absorption peak emerges. This GSB band is considered as the similar origins of band-tail or additional absorptions as previously discussed in steady absorption spectra. However, species related to these signals should be harmful to radiatively excitonic transitions, which can be regarded as the quenchers for emission. These results also suggest that quenchers are stable under strong optical excitations and might also be thermally stable since the strong pump power will also generate a significant heating effect. Interestingly, this work shows that by PMMA treatment, the formation of species related to band-tail absorptions can be greatly suppressed. For the sample with PMMA coatings, the discrepancy between the low-pump and high-pump fluences is much smaller. Stable negative absorption bands at 515, 526 and 547 nm can be seen for both low-pump and high-pump fluences, supporting that the samples with perovskite/PMMA bilayers are much more stable and have a higher laser-induced damage threshold (LIDT).

Besides, due to the refractive index of PMMA (1.48) being close to that of the quartz glass substrate (~ 1.5), a symmetric waveguides (SWGs) structure could be formed. The refractive index of the CsPbBr_3 perovskite at 534 nm is about 1.91.³⁴ Thus, the samples containing a PMMA layer possess an additional dielectric confinement factor compared with pristine CsPbBr_3 film. The waveguides structure for the pristine CsPbBr_3 sample can be regarded as asymmetric waveguides (AWGs) due to the less refractive index of air in contrast to PMMA. To investigate the differences in the confinement ability of SWGs, diagrams are shown in Figs. 5 and S4. The electric field intensity in AWGs structure moves towards the upper-cladding side (i.e., air) [Fig. 5(c)]. For the SWGs structure, the field peak intensity matches better with the center of the perovskite layer [Fig. 5(d)]. For generating

efficient ASE, it is critical to obtain the optimal confinement factor (Γ) of the transmitted mode inside the optical gain layer.³⁵ The confinement factor of a guided mode³⁶ in one-dimensional planar waveguides structure is given by³⁷

$$\Gamma = \frac{\int_{-\frac{l}{2}}^{\frac{l}{2}} s dx}{\int_{-\infty}^{+\infty} s dx} \quad (1)$$

where l is the thickness of perovskite layer, S is the Poynting vector intensity and Λ is the effective absorption length ($\Lambda = \frac{1}{\alpha_{\text{abs}}} \approx 90 \text{ nm}$,³⁸ in which α_{abs} is the absorption coefficient at the pump wavelength).³⁹ Note that since $\Lambda > l$ (80 nm), so integration of the active layer is taken across the total perovskite layer thickness. As is shown in Table S2, the confinement factor of TE_0 mode at 534 nm for AWGs is 31%, but that for SWGs is higher and beneficial to ASE.

Based on the simulation model as shown in Fig. S5, we also use the transfer matrix method to calculate the optical effect of the SWGs structure on the light in-coupling ratio (η_{in}) of excitation process at 400 nm, the out-coupling ratio (η_{out}) of emission process at 522 nm and total coupling ratio (η_{total}), where $\eta_{\text{total}} = \eta_{\text{in}} * \eta_{\text{out}}$. The results are plotted in Fig. S6. In contrast to the sample without PMMA coating, η_{total} is obviously increased with a proper thickness of PMMA coating. The PL intensity is mainly determined by the quenching channels of the excitons and η_{total} , in which the former can be revealed by τ_{avg} in PL decay measurement. As shown in Fig. S6c, the dependence of η_{total} on PMMA thickness exhibits a sinusoidal shape. However, the product of $\eta_{\text{total}} * \tau_{\text{avg}}$ versus the PMMA thickness (Fig. S6d) gives a similar hump-like shape as PL enhancement factor (Fig. 2c). Similar results were also verified at the ASE wavelength of 534 nm. These results indicate that introduction of PMMA not only plays the role of trap passivation but also results in the electric field confinement and higher light out-coupling efficiency by the SWGs structure. This is beneficial for achieving efficient ASE with lower threshold pump energy densities.

ASE properties were studied by using an 800-nm femtosecond laser with 1 kHz repetition as the excitation source (using a $\beta\text{-BaB}_2\text{O}_4$ crystal to generate 400 nm laser). Under high excitation fluences, it is clear to identify the transformation from steady-state PL to ASE. In one-photon excitation

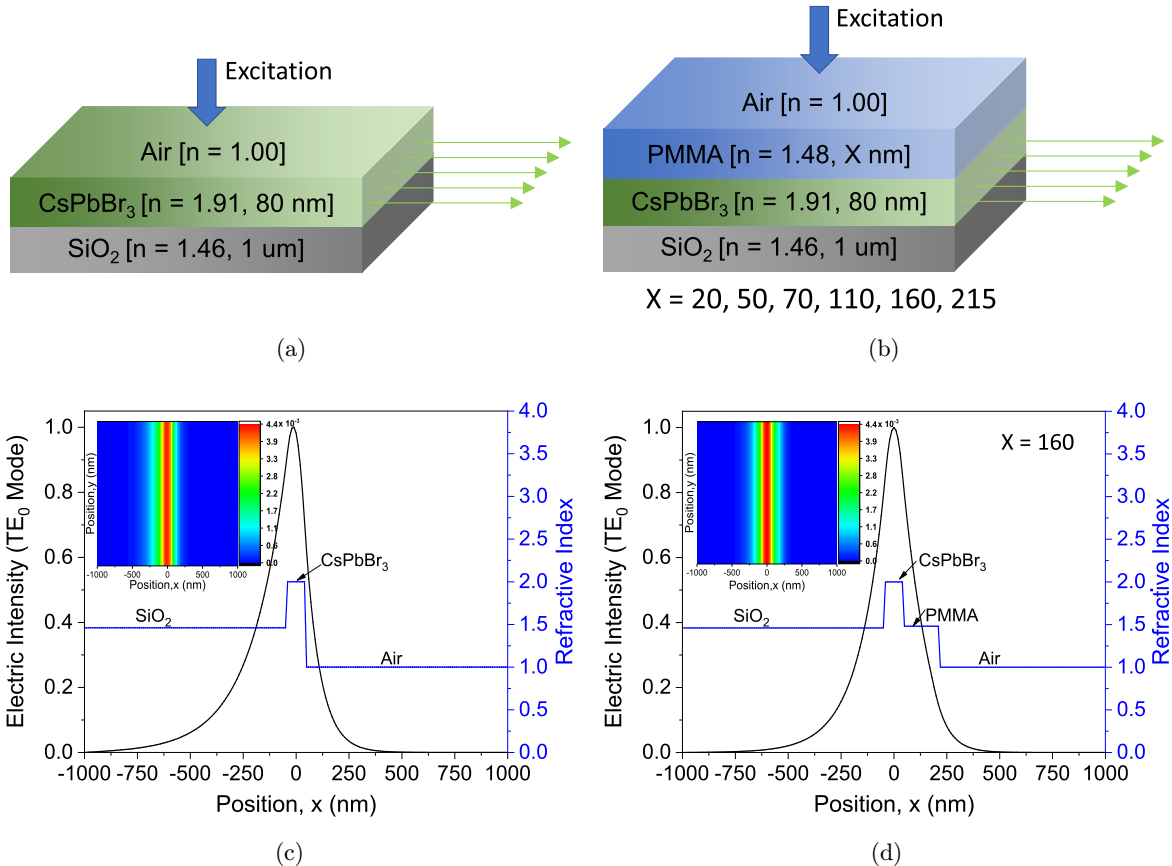


Fig. 5. Schematic of asymmetric (a) and symmetric (b) waveguide structures. Refractive index profile (blue curve) and calculated electric field intensity distribution (black curve) of TE₀ mode for AWGs (c) and SWGs (d) at 534 nm versus position. Inset: Contour map of Poynting vector (Px) versus position, showing density of power flowing through the waveguides.

conditions, the PL peak shifts from 522 nm to 534 nm, followed by the change of FWHM from 18 nm to 6 nm, which is in agreement with previous results.^{28,40} Compared to the bare CsPbBr₃, the CsPbBr₃/PMMA bilayersamples exhibit enhanced ASE intensities and reduced thresholds. The one-photon ASE spectra of bare CsPbBr₃ and CsPbBr₃/PMMA (160 nm) are shown in Fig. 6 (see Fig. S7 for other samples). The ASE threshold fluence of CsPbBr₃/PMMA (160 nm) [Fig. 6(b)] is about 30.7 $\mu\text{J}/\text{cm}^2$, which is lower than half value of the bare CsPbBr₃ [Fig. 6(a)]. The same results are also obtained at two-photon excitation. The ASE threshold fluence of CsPbBr₃/PMMA (160 nm) in Fig. 6(e) is about 7.2 mJ/cm², which is 35% lower than that of the bare CsPbBr₃ in Fig. 6(d) (see Fig. S8 for other samples). Meanwhile, due to its large two-photon absorption (2PA) cross-section,³¹ both reductions prove that the PMMA coating can enhance ASE performance of CsPbBr₃ thin films in not only one-photon but also two-photon excitation

conditions.

The ASE threshold and intensity slope as a function of the thickness of all samples in 1PPL and 2PPL conditions under respective ASE threshold fluence are shown in Figs. 6(e) and 6(f). It is worth noting that the best ASE performance happens at CsPbBr₃/PMMA (160 nm), which has a relatively lowest threshold and biggest slope. The thickness of PMMA is critical to the ASE enhancement of its coated perovskite. The optimum thickness of PMMA for ASE is shifted in contrast to the fluorescence emission, which is attributed to the higher pump energy densities for ASE devices. When the thickness of PMMA is thin, the SWGs contribution can be ignored and the passivation becomes dominant. However, if the PMMA layer is too thick, the passivation effect decreases, and relatively higher excitation fluence will be needed.

In order to probe the differences in the stability, the ASE from bare CsPbBr₃ and CsPbBr₃/PMMA (160 nm) were continuously tested under a fluence

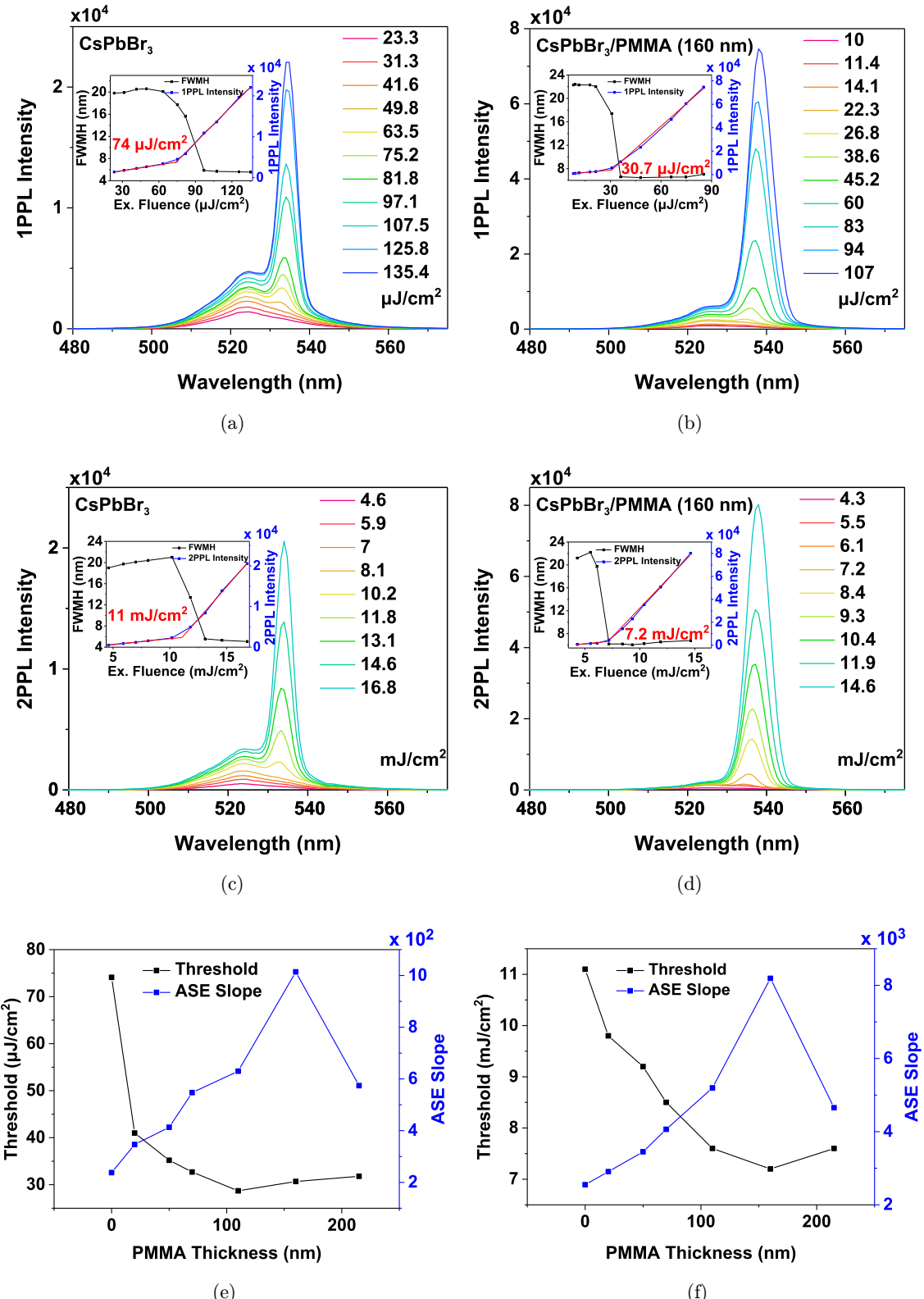


Fig. 6. (a, b) 1PPL power-dependent emission spectra from CsPbBr_3 film with and without PMMA coating, (c, d) 2PPL power-dependent emission spectra from CsPbBr_3 film with and without PMMA coating, where the inset is the FWHM and PL peak wavelength intensity versus excitation fluence and, (e, f) the threshold and ASE slope versus PMMA thickness excited by the respective threshold fluence in 1PPL and 2PPL excitation.

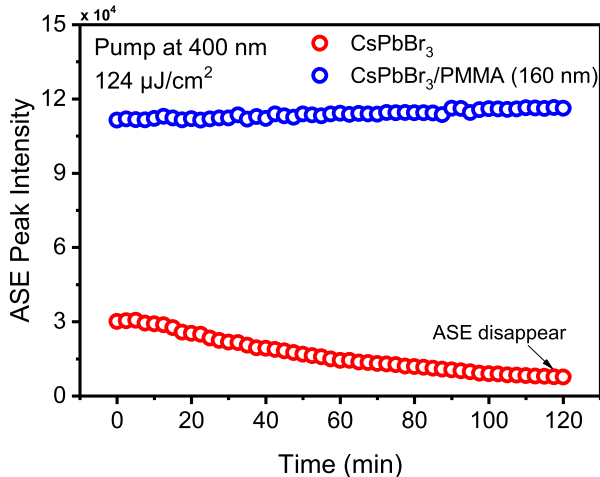


Fig. 7. ASE peak wavelength intensity stability of bare CsPbBr_3 and $\text{CsPbBr}_3/\text{PMMA}$ (160 nm).

of $124 \mu\text{J}/\text{cm}^2$ at 400 nm. As shown in Fig. 7, the ASE peak wavelength intensity of bare CsPbBr_3 decreases gradually and ASE totally disappears after about 115 min. During this period, the ASE intensity of $\text{CsPbBr}_3/\text{PMMA}$ (160 nm) remains nearly constant. The significantly enhanced lifetime by introducing the PMMA capped layer is considered resulting from several combined factors. As suggested by the spectroscopic measurement, the PMMA can passivate the trap sites, which should be beneficial for improving the stability; PMMA can also immerse into the boundaries of perovskite crystals, leading to better phase stability. At a higher excitation fluence, the concentration quenching effect in PMMA-containing samples is greatly suppressed, as indicated by femtosecond TA measurement. This can dramatically enlarge the stability performances for the cases without and with a PMMA encapsulated layer. Finally, the PMMA can block the invasion of water, oxygen in the air, which should also be helpful for a better operational lifetime.

4. Conclusion

In conclusion, we have demonstrated the feasibility of enhancing one-photon and two-photon spontaneous emissions and ASE of CsPbBr_3 by simply coating an insulating PMMA layer with an optimized thickness on top. It is disclosed that the thickness of the PMMA layer has a vital effect on spontaneous emission and ASE performances. A variety of spectroscopic methods such as XRD, steady-state and transient absorption and PL were

adopted to investigate the effectiveness of the insulating layer. The enhancement was attributed to the trap passivation and electric field restraint due to the dielectric confinement by the formation of SWGs structure. Moreover, under intense pump irradiation, the perovskite films with PMMA coating show much better ASE stability than the control device. Our results might suggest the potential of a general method by introducing transparent and insulating polymers in developing efficient and stable two-photon perovskite lasers.

References

- X. Xiao, M. Wu, Z. Ni, S. Xu, S. Chen, J. Hu, P. N. Rudd, W. You and J. Huang, *Adv. Mater.* **32**, 2004080 (2020).
- J. Ding, Z. Lian, Y. Li, S. Wang and Q. Yan, *J. Phys. Chem. Lett.* **9**, 4221 (2018).
- Z. Z. Liu, Z. P. Hu, Z. Y. Zhang, J. Du, J. Yang, X. S. Tang, W. M. Liu and Y. X. Leng, *Acs Photonics* **6**, 3150 (2019).
- W. Xu, Q. Hu, S. Bai, C. Bao, Y. Miao, Z. Yuan, T. Borzda, A. J. Barker, E. Tyukalova, Z. Hu, M. Kawecki, H. Wang, Z. Yan, X. Liu, X. Shi, K. Uvdal, M. Fahlman, W. Zhang, M. Duchamp, J.-M. Liu, A. Petrozza, J. Wang, L.-M. Liu, W. Huang and F. Gao, *Nat. Photon.* **13**, 418 (2019).
- Y. Cao, N. Wang, H. Tian, J. Guo, Y. Wei, H. Chen, Y. Miao, W. Zou, K. Pan, Y. He, H. Cao, Y. Ke, M. Xu, Y. Wang, M. Yang, K. Du, Z. Fu, D. Kong, D. Dai, Y. Jin, G. Li, H. Li, Q. Peng, J. Wang and W. Huang, *Nature* **562**, 249 (2018).
- T. Watanabe, T. Yamanari and K. Marumoto, *Commun. Mat.* **1**, 96 (2020).
- C. Bao, W. Xu, J. Yang, S. Bai, P. Teng, Y. Yang, J. Wang, N. Zhao, W. Zhang, W. Huang and F. Gao, *Nat. Electronics* **3**, 156 (2020).
- G. Xing, N. Mathews, S. S. Lim, N. Yantara, X. Liu, D. Sabba, M. Gratzel, S. Mhaisalkar and T. C. Sum, *Nat. Mater.* **13**, 476 (2014).
- S. Yakunin, L. Protesescu, F. Krieg, M. I. Bodnarchuk, G. Nedelcu, M. Humer, G. De Luca, M. Fiebig, W. Heiss and M. V. Kovalenko, *Nat. Commun.* **6**, 8056 (2015).
- Q. Shang, M. Li, L. Zhao, D. Chen, S. Zhang, S. Chen, P. Gao, C. Shen, J. Xing, G. Xing, B. Shen, X. Liu and Q. Zhang, *Nano Lett.* **20**, 6636 (2020).
- Y. Mi, Y. Zhong, Q. Zhang and X. Liu, *Adv. Opt. Mater.* **7**, 1900544 (2019).
- H. Zhu, Y. Fu, F. Meng, X. Wu, Z. Gong, Q. Ding, M. V. Gustafsson, M. T. Trinh, S. Jin and X.-Y. Zhu, *Nat. Mater.* **14**, 636 (2015).

13. H. Yu, X. Xu, H. Liu, Y. Wan, X. Cheng, J. Chen, Y. Ye and L. Dai, *ACS Nano.* **14**, 552 (2020).
14. Y. Wang, X. Li, J. Song, L. Xiao, H. Zeng and H. Sun, *Adv. Mater.* **27**, 7101 (2015).
15. C. Qin, A. S. D. Sandanayaka, C. Zhao, T. Matsushima, D. Zhang, T. Fujihara and C. Adachi, *Nature* **585**, 53 (2020).
16. Q. Sun and W.-J. Yin, *J. Am. Chem. Soc.* **139**, 14905 (2017).
17. S. Q. Li, D. Y. Lei, W. Ren, X. Y. Guo, S. F. Wu, Y. Zhu, A. L. Rogach, M. Chhowalla and A. K. Y. Jen, *Nat. Commun.* **11**, 1192 (2020).
18. R. Wang, M. Muhammad, Y. Duan, Z.-K. Wang, J. Xue and Y. Yang, *Adv. Funct. Mater.* **29**, 1808843 (2019).
19. F. Wang, M. Endo, S. Mouri, Y. Miyauchi, Y. Ohno, A. Wakamiya, Y. Murata and K. Matsuda, *Nanoscale* **8**, 11882 (2016).
20. D. Bi, C. Yi, J. Luo, J.-D. Décoppet, F. Zhang, Shaik M. Zakeeruddin, X. Li, A. Hagfeldt and M. Grätzel, *Nat. Energy* **1**, 16142 (2016).
21. J. Yang, S. Xiong, T. Qu, Y. Zhang, X. He, X. Guo, Q. Zhao, S. Braun, J. Chen, J. Xu, Y. Li, X. Liu, C. Duan, J. Tang, M. Fahlman and Q. Bao, *ACS Appl. Mater. Interfaces* **11**, 13491 (2019).
22. A. Pan, L. Yan, X. Ma, Y. Wu, Y. Zhang, G. Zhou and L. He, *J. Alloy. Compd.* **844**, 156102 (2020).
23. J. He, J. Liu, Y. Hou, Y. Wang, S. Yang and H. G. Yang, *Nat. Commun.* **11**, 4237 (2020).
24. X. Li, M. Ibrahim Dar, C. Yi, J. Luo, M. Tschumi, S. M. Zakeeruddin, M. K. Nazeeruddin, H. Han and M. Grätzel, *Nat. Chem.* **7**, 703 (2015).
25. C.-G. Lu, X.-F. Hu, S.-H. Xu, H.-G. Liu, J.-K. Xu, Y.-P. Cui and C.-L. Wang, *RSC Adv.* **10**, 25480 (2020).
26. M. Jin, S. Huang, C. Quan, X. Liang, J. Du, Z. Liu, Z. Zhang and W. Xiang, *J. Eur. Ceram. Soc.* **41**, 1579 (2021).
27. L. Lei, S. Dovletgeldi, D. Qi, S. Samuel, H. Siliang, M. Juliana, W. A. Harald, G. Kenan and S. Franky, presented at *Proc. SPIE XXIV*, 1147312 (2020).
28. C. L. Li, Z. G. Zang, C. Han, Z. P. Hu, X. S. Tang, J. Du, Y. X. Leng and K. Sun, *Nano Energy* **40**, 195 (2017).
29. N. Pourdavoud, T. Haeger, A. Mayer, P. J. Cegielski, A. L. Giesecke, R. Heiderhoff, S. Olthof, S. Zaeffferer, I. Shutsko, A. Henkel, D. Becker-Koch, M. Stein, M. Cehovski, O. Charfi, H. H. Johannes, D. Rogalla, M. C. Lemme, M. Koch, Y. Vaynzof, K. Meerholz, W. Kowalsky, H. C. Scheer, P. Gorri and T. Riedl, *Adv. Mater.* **31**, e1903717 (2019).
30. L. Zhao, Y. Chen, X. Yu, X. Xing, J. Chen, J. Song and J. Qu, *J. Mater. Chem. C* **8**, 5847 (2020).
31. G. Nagamine, J. O. Rocha, L. G. Bonato, A. F. Nogueira, Z. Zaharieva, A. A. R. Watt, C. H. de Brito Cruz and L. A. Padilha, *J. Phys. Chem. Lett.* **9**, 3478 (2018).
32. S. B. Sun, D. Yuan, Y. Xu, A. F. Wang and Z. T. Deng, *Acs Nano.* **10**, 3648 (2016).
33. C. Wu, H. Li, Y. Yan, B. Chi, K. M. Felice, R. B. Moore, B. A. Magill, R. R. H. H. Mudiyanselage, G. A. Khodaparast, M. Sanghadasa and S. Priya, *Solar RRL* **2**, 1800052 (2018).
34. M. Zhao, Y. Shi, J. Dai and J. Lian, *J. Mater. Chem. C* **6**, 10450 (2018).
35. J. R. Smirnov, Q. Zhang, R. Wannemacher, L. Wu, S. Casado, R. Xia, I. Rodriguez and J. Cabanillas-Gonzalez, *Sci. Rep.* **6**, 34565 (2016).
36. M. H. Weik, Confinement factor, in *Computer Science and Communications Dictionary*, doi: 10.1007/1-4420-0613-6-3532 (Ed: M. H. Weik), (Springer, US, Boston, MA) 2001, p. 285.
37. I. B. Martini, I. M. Craig, W. C. Molenkamp, H. Miyata, S. H. Tolbert and B. J. Schwartz, *Nat. Nano.* **2**, 647 (2007).
38. J. De Roo, M. Ibanez, P. Geiregat, G. Nedelcu, W. Walravens, J. Maes, J. C. Martins, I. Van Driessche, M. V. Kovalenko and Z. Hens, *ACS Nano.* **10**, 2071 (2016).
39. W. Holzer, A. Penzkofer, T. Schmitt, A. Hartmann, C. Bader, H. Tillmann, D. Raabe, R. Stockmann and H. H. Hörold, *Opt. Quant. Electron.* **33**, 121 (2001).
40. Y. Q. Xu, Q. Chen, C. F. Zhang, R. Wang, H. Wu, X. Y. Zhang, G. C. Xing, W. W. Yu, X. Y. Wang, Y. Zhang and M. Xiao, *J. Am. Chem. Soc.* **138**, 3761 (2016).

Supporting Information

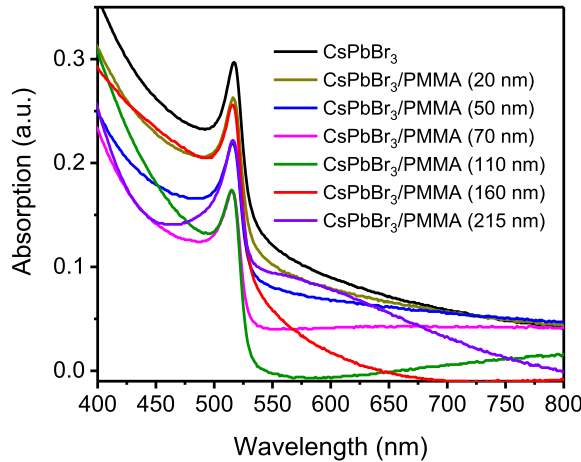


Fig. S1. Absorption spectra of CsPbBr₃ thin films without and with PMMA coating in a different thickness.

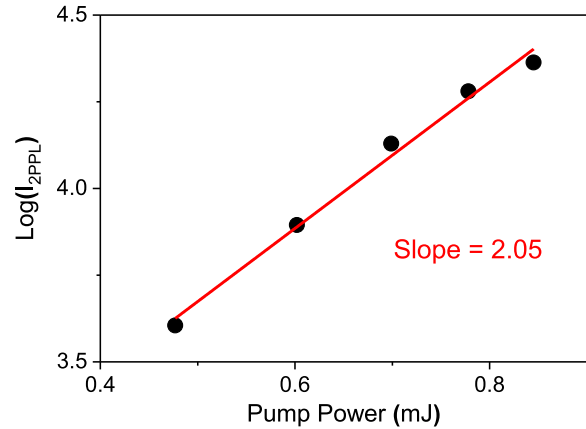


Fig. S2. 2PPL peak wavelength intensity versus pump power in CsPbBr₃/PMMA (160 nm).

Table S1. Summary of the fitting results of PL decays.

PMMA thickness (nm)	a_1 (a.u.)	τ_1 (ns)	f_1 (%)	a_2 (a.u.)	τ_2 (ns)	f_2 (%)	τ_{average} (ns)
0	132547.2	1.3 ($\pm 3.8\%$)	99.31	165.8	3.71 ($\pm 2.41\%$)	0.69	1.32 ($\pm 3.97\%$)
20	175831.5	1.19 ($\pm 2.16\%$)	97.11	2221.3	4.01 ($\pm 2.31\%$)	2.89	1.27 ($\pm 3.81\%$)
50	192004.6	1.2 ($\pm 2.93\%$)	99.13	1425.7	4.17 ($\pm 2.68\%$)	0.87	1.23 ($\pm 6.88\%$)
70	94537.5	1.54 ($\pm 2.20\%$)	91.24	4501.7	4.2 ($\pm 5.10\%$)	8.76	1.77 ($\pm 8.32\%$)
110	90453.6	1.58 ($\pm 3.84\%$)	91.55	3010.4	4.11 ($\pm 2.03\%$)	8.45	1.79 ($\pm 5.02\%$)
160	985343	1.61 ($\pm 1.24\%$)	95.71	2425.8	4.15 ($\pm 2.09\%$)	4.29	1.71 ($\pm 3.21\%$)
215	180578	1.21 ($\pm 2.01\%$)	96.24	2361.4	3.61 ($\pm 4.17\%$)	3.76	1.31 ($\pm 6.21\%$)

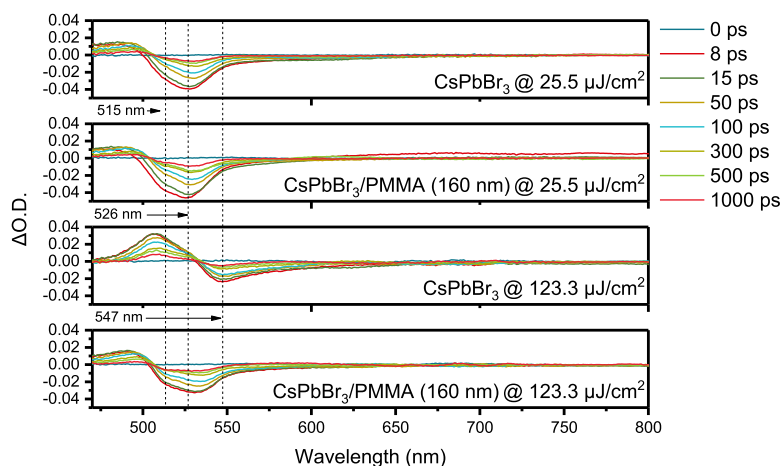


Fig. S3. Spectral evolution curves of femtosecond transient absorption of CsPbBr₃ pumped under a fluence of (a) $25.5 \mu\text{J}/\text{cm}^2$ and (c) $123.3 \mu\text{J}/\text{cm}^2$, and CsPbBr₃/PMMA (160 nm) pumped under a fluence of (b) $25.5 \mu\text{J}/\text{cm}^2$ and (d) $123.3 \mu\text{J}/\text{cm}^2$, respectively.

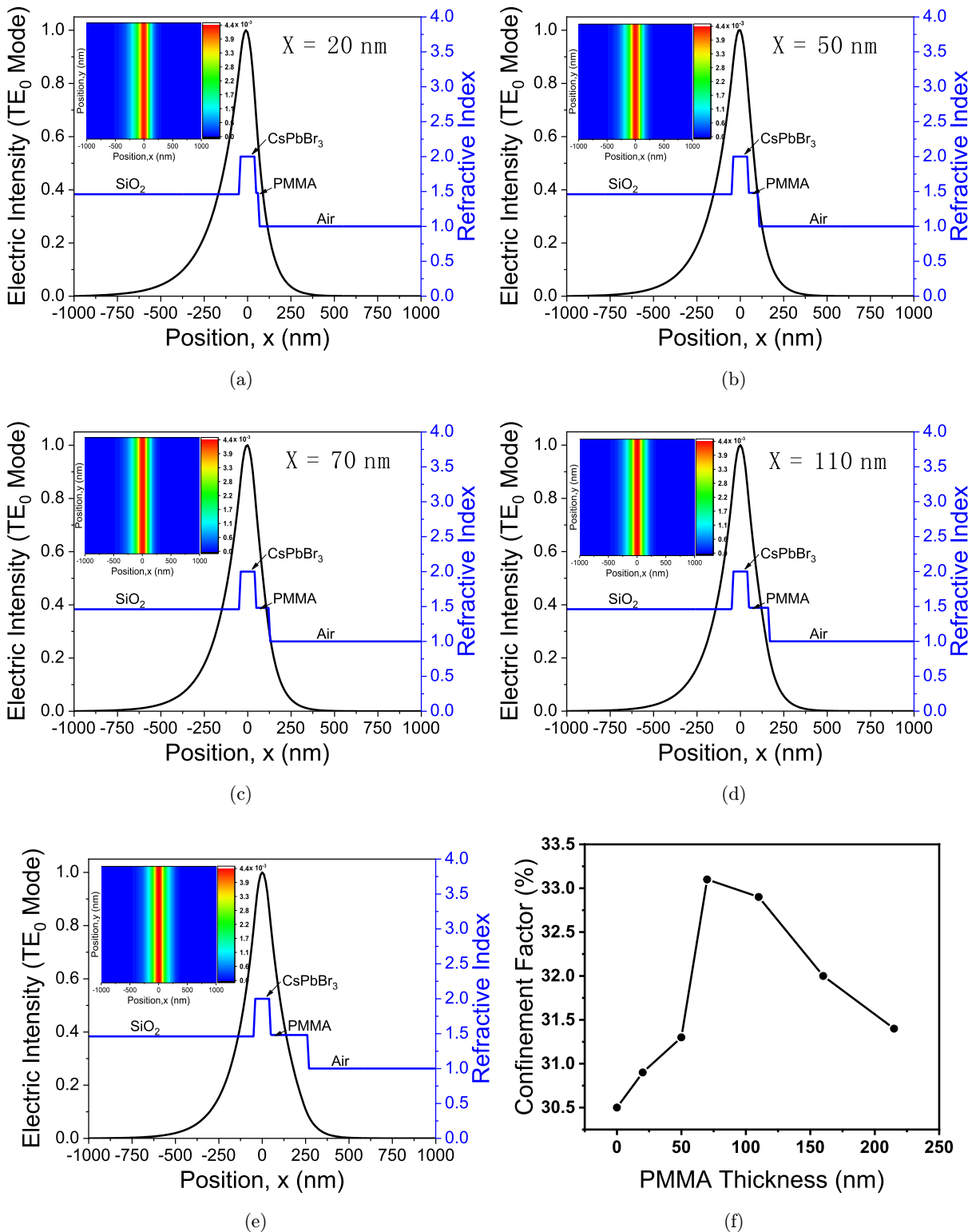


Fig. S4. (a–e) Electric field intensity distribution, inset: Contour map of Poynting vector (P_x) versus position, showing density of power flowing through the waveguides, (f) confinement factor versus PMMA thickness.

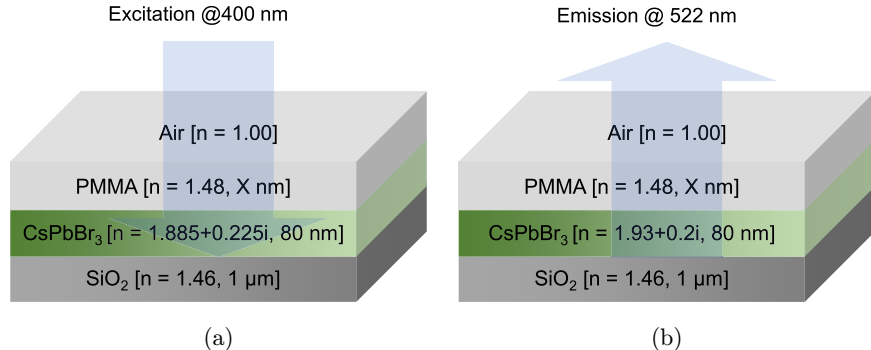


Fig. S5. Optical simulation of light coupling ratio of (a) the excitation (400 nm) process from air to CsPbBr_3 through different thickness of PMMA, (b) the emission (522 nm) process from CsPbBr_3 to air through different thickness of PMMA. While $X = 0, 20, 50, 70, 110, 160, 215$, respectively.

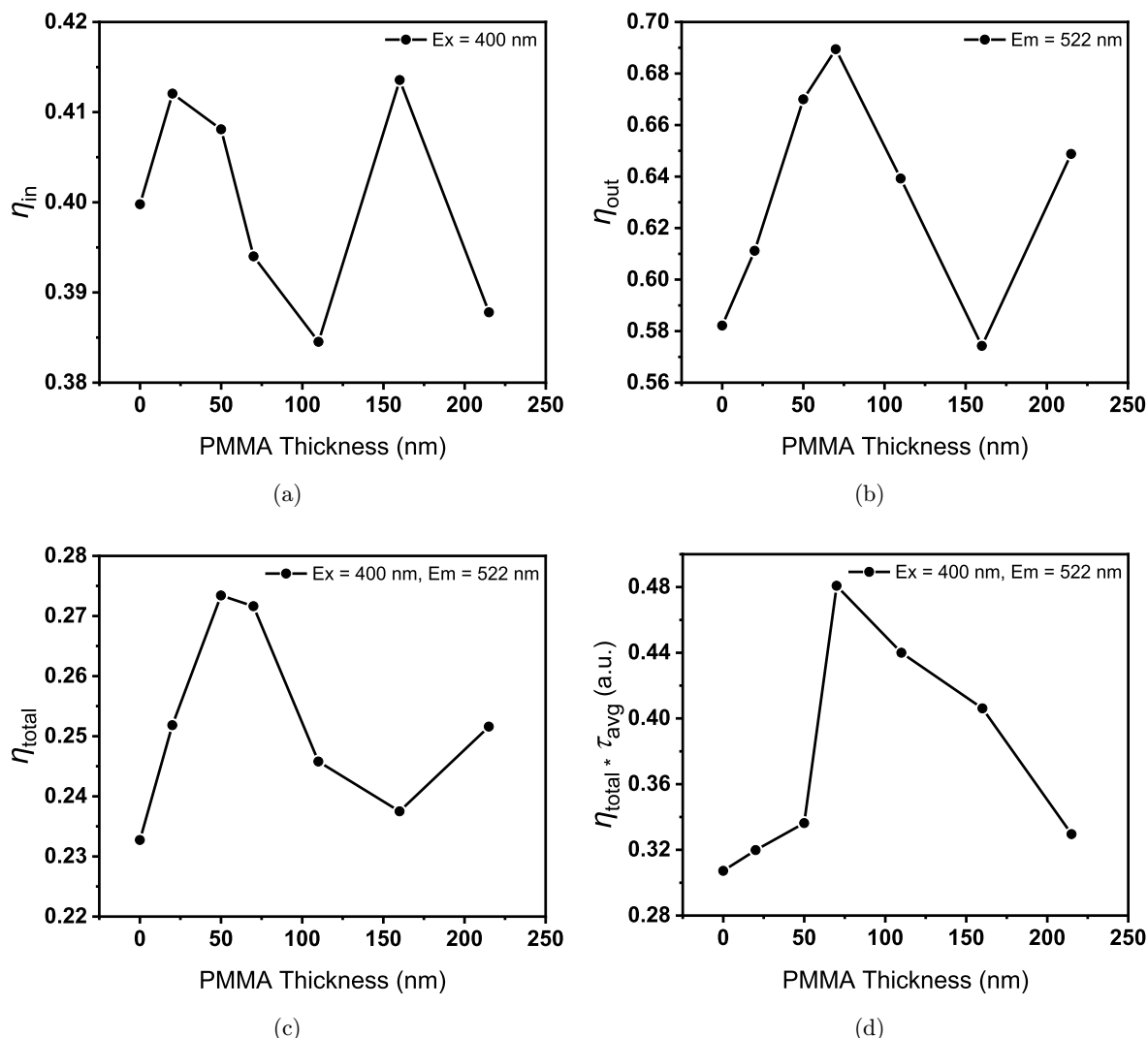
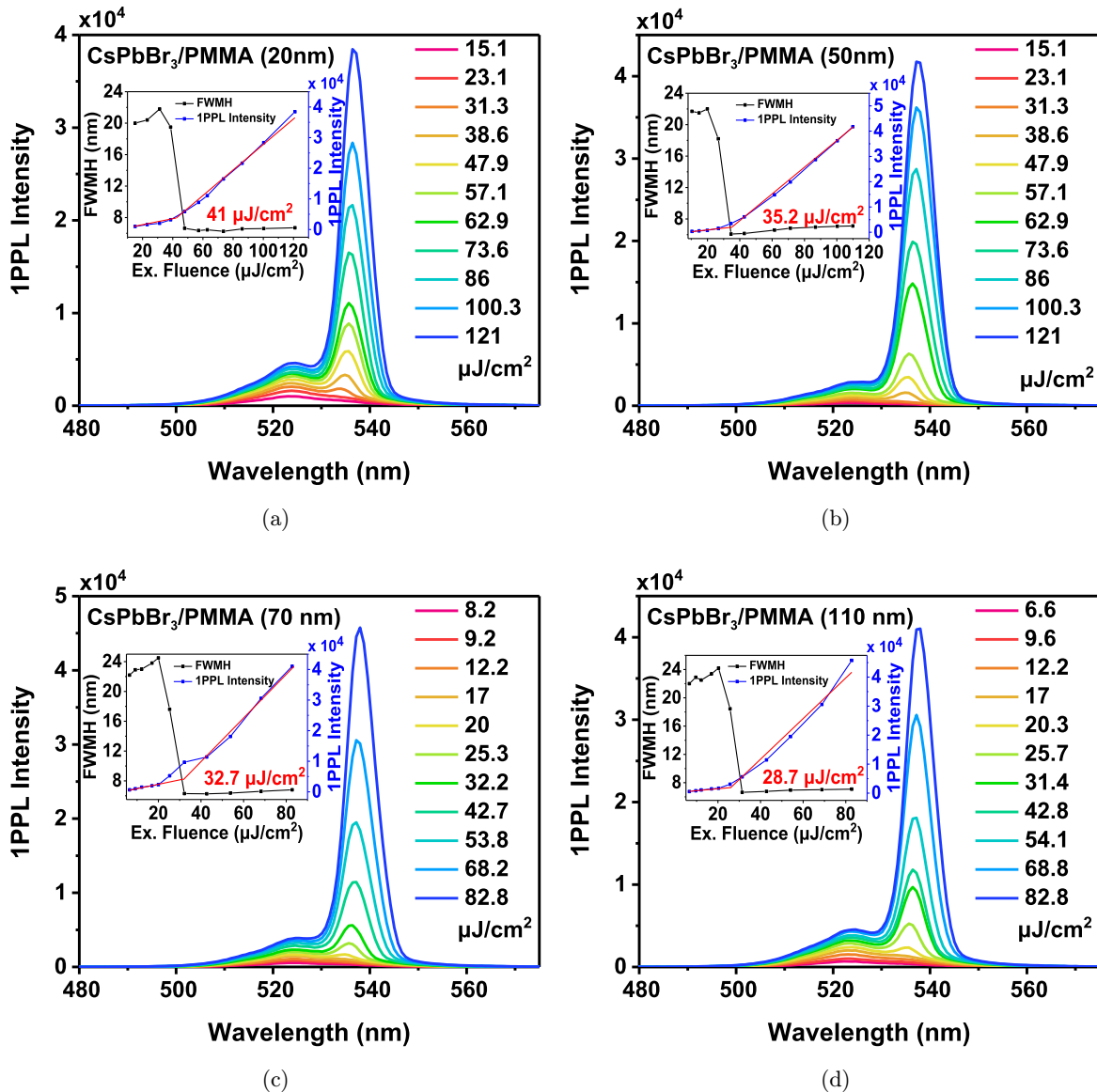


Fig. S6. (a) In-coupling ratio (η_{in}) of excitation (400 nm) from air to CsPbBr_3 through different thickness of PMMA, (b) out-coupling ratio (η_{out}) of emission (522 nm) from CsPbBr_3 to air through different thickness of PMMA and (c) total coupling ratio ($\eta_{\text{total}} = \eta_{\text{in}} \times \eta_{\text{out}}$), (d) $\eta_{\text{total}} * \tau_{\text{avg}}$ versus PMMA thickness.

Table S2. Summary of the confinement factor (Γ) of TE_0 mode.

PMMA Thickness (nm)	0	20	50	70	110	160	215
Confinement Factor (%)	30.5	30.9	31.3	33.1	32.9	32	31.4

Fig. S7. (a-e) 1PPL (400 nm, 1 kHz, 120 fs) power-dependent emission spectra from CsPbBr_3 film coating with different thickness of PMMA, (f) 1PPL intensity of CsPbBr_3 film with a variety of thickness of PMMA under different excitation fluence.

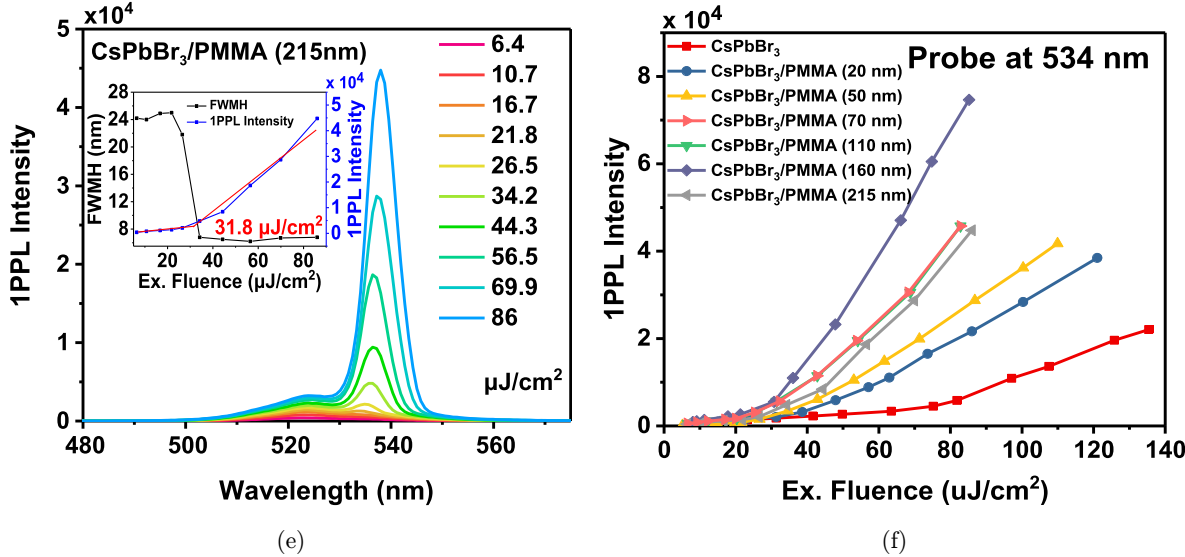


Fig. S7. (Continued)

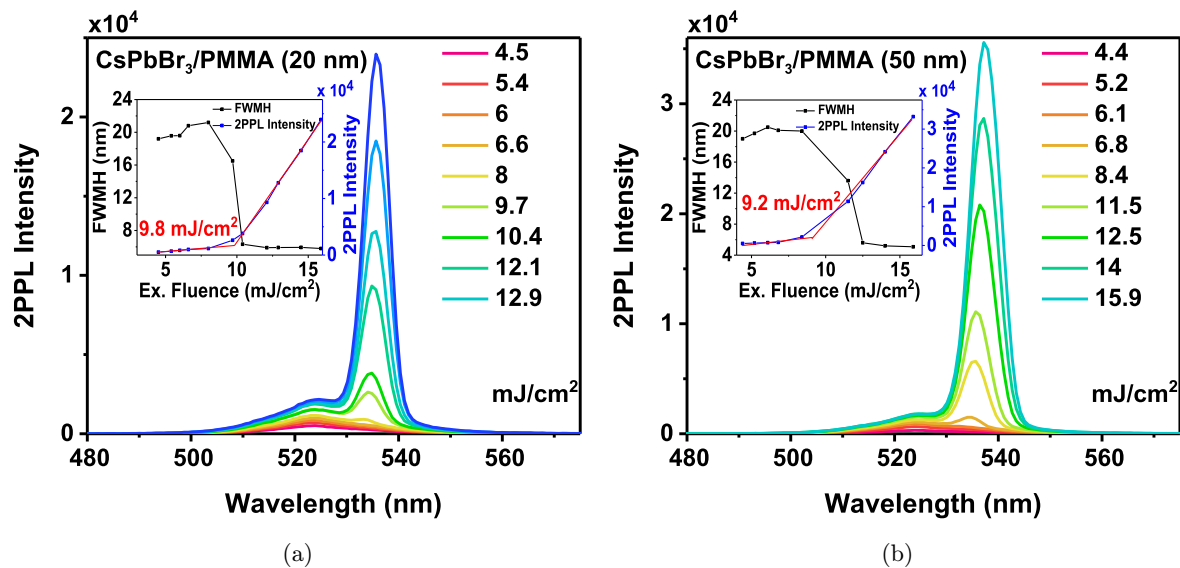


Fig. S8. (a-e) 2PPL (800 nm, 1 kHz, 120 fs) power-dependent emission spectra from CsPbBr₃ film coating with different thickness of PMMA, (f) 2PPL intensity of CsPbBr₃ film with a variety of thickness of PMMA under different excitation fluence.

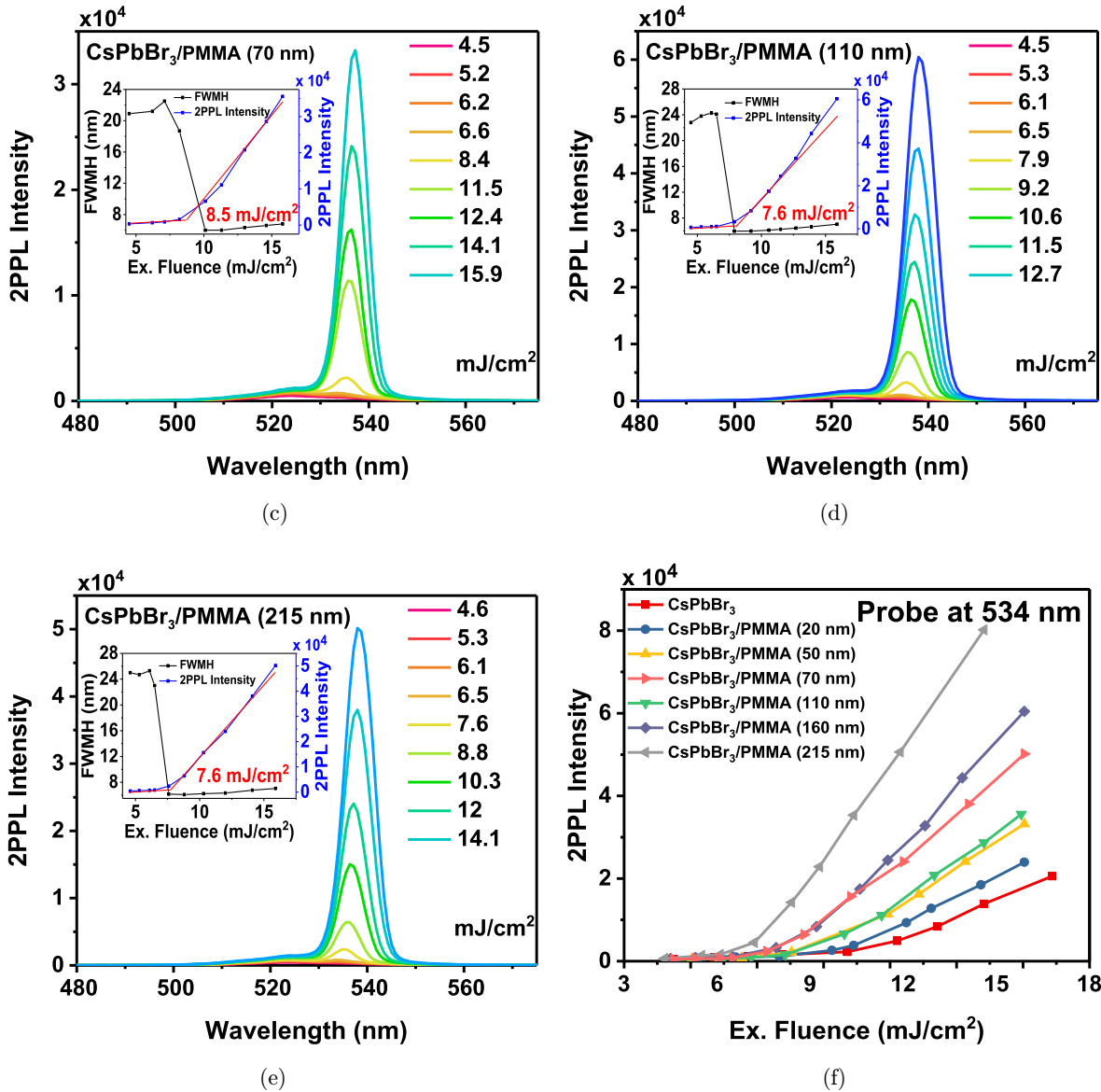


Fig. S8. (Continued)